International Journal of Thermal Sciences 48 (2009) 1696–1706

Contents lists available at ScienceDirect

International Journal of Thermal Sciences

journal homepage: www.elsevier.com/locate/ijts

Superficial heat transfer by forced convection and radiation in a horizontal channel

Yassine Cherif, Annabelle Joulin*, Laurent Zalewski, Stéphane Lassue

Laboratoire d'Artois de Mécanique Thermique et Instrumentation (LAMTI), Faculté des Sciences Appliquées, Université d'Artois, Technoparc Futura, 62400 Béthune, France

ARTICLE INFO

Article history:
Received 2 April 2008
Received in revised form
3 December 2008
Accepted 26 January 2009
Available online 23 March 2009

Keywords:
Superficial heat transfer
Turbulent forced convection
Heat flux sensor
3D numerical simulation

ABSTRACT

This paper presents a numerical investigation of turbulent forced convective flow in a horizontal channel. An exchanger isothermal test plate is embedded in the lower wall, in the fully developed region of the flow close to the exit of the channel. Above this isothermal plate, on the upper surface, a black coated isothermally heating resistance facing downwards is installed. This absorbing surface provides a controlled radiative heat flux on the lower test plate. In this study, custom-built tangential gradient fluxmeters (TGFM) are used to provide local measurements of convective heat transfer so as to validate the numerical predictions. Then, parametric studies are carried out. The profiles for the heat flux are presented for different Reynolds numbers in the flow direction along the cold isothermal lower plate. Then, the influence of the presence of an obstacle, located on the lower surface, on the heat flux is also investigated. All numerical predictions are carried out with Fluent, previously calibrated against benchmark problems and experimental measurements. In the paper, special emphasis is given in the systematic comparison between experimental and numerical results.

1. Introduction

In many fields the knowledge and the control of transferred heat flux are essential for optimum operation of systems, both in terms of efficiency and energy savings. Heat transfer at a wall surface is studied in various energy related fields, such as the cooling of electronic components, air conditioning in buildings, and, in general, the effectiveness of heat exchangers. One of the main problems in such situations is assigning a coherent value to the heat transfer coefficient between the wall surface and a fluid [1]. This coefficient is sometimes simplified using a linearizing transfer. For example, the model used here is a simple model called "Newton's law of cooling", where the transferred heat flux is estimated to be proportional to the existing temperature difference between the heat transfer surface and the fluid [2,3].

The heat exchange transfer coefficient is dependent on many parameters (geometry, fluid, temperature levels, etc.). Various techniques were studied and used to obtain correlations for the calculation of this coefficient. Although the temperatures can usually be measured without any problem, determining the magnitude of the heat flux is not obvious. Experimental methods are generally based on the measurement of temperatures. This intensive magnitude, measured at a given instant, provides few information on the system's evolution. Experimental methods are often based on a non-stationary state generation. But in this case, the use of a constant heat transfer coefficient is questionable. The main problem arises from the assumption that the heat transfer coefficient h is constant because, the system is thermally non-stationary to allow detecting temperature variations [4–6]. We thus consider that it hardly varies.

Another method called the Flash method [7–10] consists on thermally perturbing the exchanged surface by means of a radiant energy source. The study of the temperatures temporal decrease until an equilibrium state provides the superficial exchanged conditions. In this method, infrared thermography is an interesting alternative [11–14] in the case where the surface radiative properties, the fluid influence on radiative transfer, and the radiative environment of the experimental apparatus are known [15,16]. The thermogram treatment and its interpretation yield to characterize the exchange. This apparatus is particularly heavy and costly. It needs lots of precautions to be really efficient. It is not generalized to all the convection heat transfer problems.

The surface component can be locally equipped with temperature probes on and below the surface. Knowing the wall material thermo-physical properties, and by means of inverse methods [17–19], it can be possible to get the superficial exchange [20,21]. In this case, the flow perturbation is very weak if thermocouples insertion is realized with many precautions. Other methods exist,

* Corresponding author. Tel.: +33 321 632356; fax: +33 321 632366.
E-mail address: annabelle.joulin@univ-artois.fr (A. Joulin).

1290-0729/$ – see front matter © 2009 Elsevier Masson SAS. All rights reserved.
doi:10.1016/j.ijthermalsci.2009.01.017

consisting on depositing a coating sensitive to the surface temperature. It could be liquid cristal that reflects different colors according to their temperature [22,23], or materials which are the places of mass transfer or chemical reactions (NH_3 and $MnCl_2$) [24]. The interpretation is delicate and the accuracy remains weak. These experimental methods are limited to temperatures adapted to the coating properties, and the material life is also very short.

Other authors have tried to directly obtain the exchanged thermal flux magnitude. To do this, measurement tools are more or less sophisticated.

There are many types of heat flux sensors [25,26]; their principle of operation is mostly based on the "seaming" of thermocouples through an auxiliary wall with a known heat resistance. In this case, their thickness (a few mm) and their effect on the measurement may be non-negligible [27].

Another type of sensor is the active fluxmeter, embedded in the wall, for which a power setting allowing a constant wall temperature offsets losses by conduction. In the case of convection measurement, this dissipative fluxmeter has been recently used and provides good results for measures within the flow [25]. However, measures upon the surface do not seem possible without local exchange perturbation.

Several thermal flux sensors have been carried out and are based on thermo-electrical effects [25,26].

A large number of methods used to measure the heat flux is based on the temperature measures on the surface or close to the surface of a solid. Usually, this includes an experimental device generating a physical perturbation. As with any probe, it is necessary to reduce the perturbation caused by the presence of this probe. It is thus particularly important to understand these intrusive effects that have an influence on the measured value accuracy.

We briefly describe here several fluxmeters to understand the advantages of ours. First, we can cite the unidimensional plane sensor. Ortolano and Hines [28] have proposed a simplified model of this fluxmeter. Two metal foils are alternately wrapped around a thin plastic foil (Kapton) and joined on each side to form the thermo-electrical junctions of the thermocouple. With this type of sensor, the response time is under 20 ms, but transient signal can be reduced unless the frequency of the perturbation is less than several Hertz.

A device of similar design uses a joined wire to form a thermopile across a 1 mm thickness probe has been described by Ochaoa [29]. This yields a higher sensibility for the heat flux and increases its thermal resistance. Time constants are about 1 s and the upper limit of temperature to be used is about 300 °C allowing a wide range of applications in thermal transfer.

This present article reports on a project to test a device that enables the accurate measurement of convective heat transfer coefficients. The first objective of this paper is to show how it is possible to separate these heat transfer components by means of our experimentation. The second objective is aimed at determining the evolution of the flux in the flow direction. Finally, the last experiment shows the change in heat transfer behind a rectangular obstacle placed in the channel. Two methodological approaches are adopted to investigate the air flow and the heat transfer in this duct: experimental measurements on the one hand and 3D numerical simulations on the other hand.

2. Physical problem and experimental setup

2.1. Description of fluxmeters

The fluxmetric sensors used in this work [30] were developed a few years ago in our laboratory. They are qualified as tangential gradient flux sensors because their internal structure allows generating temperature gradients between thermoelectric junctions in the sensor plane (Fig. 1(a)). This allows reducing thickness ($\sim$200 μm), while providing a good sensitivity ($\sim$100 μV/W/m^2) for a sensor 15 × 15 cm^2. It is the main advantage, hence minimal disturbance caused by its presence on the system is to be studied.

Many tangential gradient plated thermocouples are incorporated in these fluxmeters. This type of fluxmeters is produced using printed circuit technology.

The construction principle of the sensor is: a constantan strip is placed on a Kapton support and copper elements are electrolytically deposited on the strip (Fig. 1(a)). Conducting "wedges" constrict the heat transfer lines traversing the sensor plane. A temperature difference tangential to the measurement plane then appears between the extremities of the copper deposits. As a result, a Seebeck emf is generated across the terminals of the plated thermocouples. These elements are mounted in series to allow a non-negligible emf proportional to the heat flux traversing the sensor plane at the extremities of the constantan strip.

Two conducting foils (aluminum or copper) are glued to each of the sensor sides to ensure the uniformity of the surface temperatures. The heat transfer lines are unidirectional with respect to the inlet and outlet surfaces of the sensor measurement area and the supplied signal is independent of the material on which the fluxmeter is placed. Precautions are taken to ensure unidirectional thermal flow through the fluxmeter and the independance of its sensitivity with respect to the thermo-physical properties of the material on which it was laid. The disturbance due to the sensor's presence is reduced, and these sensors are flexible and can be used on curved surfaces (pipes, etc.), which increases their field of application. The empty spaces between the wedges are filled with resin, making negligible sensor sensitivity variations in comparison to temperature and pressure in the application fields of interest

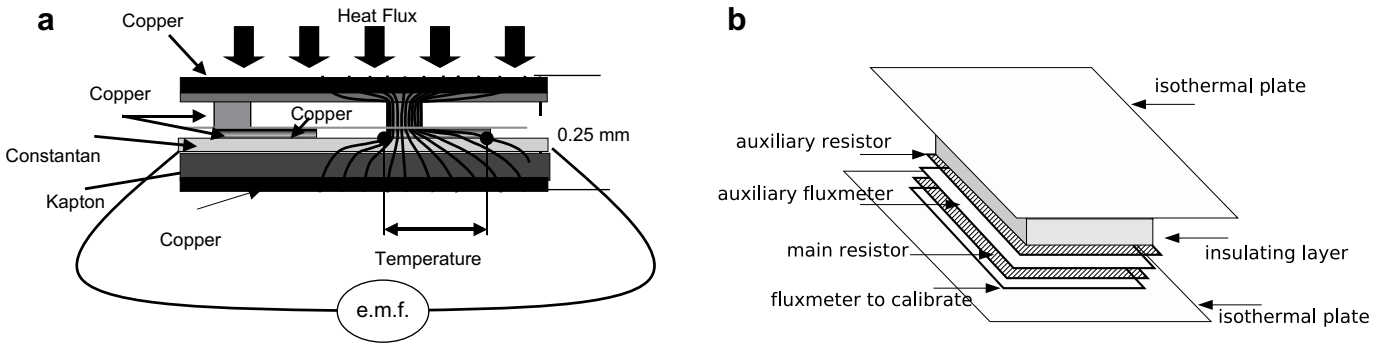

Fig. 1. Schematic drawing of heat flux sensors (a) Heat flux sensor's sketch (b) Calibration apparatus.

(temperatures of −50 °C and +150 °C and pressures less than 5 bars).

2.1.1. Calibration

The calibration of a fluxmeter is performed in order to determine its sensitivity and to study its response versus thermal solicitations. Several methods are available [31]. The secondary transducer method was carried out [32,33]. The advantage of this method resides in the possibility to control the thermal equilibrium by means of another uncalibrated fluxmeter. The set up chosen for calibration is depicted in Fig. 1(b). The fluxmeter to be calibrated is placed on an isothermal cold plate. It is covered by a heat main resistor, an uncalibrated fluxmeter and an auxiliary resistance, of same dimensions. On the top of this system, an insulating layer is installed in order to reduce heat losses. To ensure a perfect contact between these different elements, a heavy solid is placed on the top to press the pile up. The calibration process consists in the measurement of a total thermal power provided by the main heat resistor (Joule effect). The provided power P_f is absorbed by the isothermal lower plate. The lost part crossing the upper fluxmeter is balanced by the second resistor so as to get a zero heat flux. Thus, the sensitivity is given by the equation:

$$K = \frac{V \cdot S}{U \cdot I} \tag{1}$$

with $P_f = U \cdot I$, V is the voltage delivered by the sensor, U is the voltage delivered across the main resistor, I is the electric current and S is the active surface of the fluxmeter.

Antczack [31] has verified that sensitivity is independent on the flux direction. Temperature (−20 °C to + 100 °C) has a negligible influence on its sensitivity as well as pressure of a few bars applied on sensors.

2.1.2. Uncertainty analysis

Sensitivity is determined by calibration, that is, by having a heat flux traversing the active surface of the sensor on a plate at constant temperature. Since the surface density of the thermo-elements is uniform, sensitivity is directly proportional to the sensor surface. A precise method of estimating uncertainty in experimental results has been presented by Kline and McClintock. The uncertainty in the result is given in Ref. [34], and for the sensitivity K:

$$\Delta K = \left[\left(\frac{\partial K}{\partial V}\Delta V\right)^2 + \left(\frac{\partial K}{\partial S}\Delta S\right)^2 + \left(\frac{\partial K}{\partial U}\Delta U\right)^2 + \left(\frac{\partial K}{\partial I}\Delta I\right)^2\right]^{1/2} \tag{2}$$

The various terms are calculated and found to be of magnitude 1%, except for the estimation on the magnitude of the surface dimensions of the fluxmeter.

In case of a simple flow on isothermal and horizontal plates, the relative uncertainties between measured heat fluxes and calculated ones are weak, about a few percents. The uncertainties on the sensors sensitivity (approximately 3%) obtained during the calibration can be reasonably determined using the method of Kline and McClintock [34], by carefully fixing uncertainties on the measured primary variables (electric currents, resistances, voltage, and geometrical dimensions of the sensors). These sensors were laid out in hollows created into a thin and conducting plate, glued on an aluminum exchanger plate which is a thermal sink. The fluxmeters are glued with a siliconated thermal grease, the grooves remaining around sensitive areas prevent possible side heat transfer and ensure that the heat exchanged on the surface crosses the surface of measurement well, the flux lines being parallel and unidirectional both at the entry and the outlet sides of the sensor [35]. This support plate having identical properties to the ones of heat flux sensors and as the system has been covered with a uniform coating (painting), the surface is isothermal. This was checked before by using several thermocouples laid out at various positions on the plate.

2.2. Experimental apparatus

These sensors have been regularly upgraded and used particularly for investigations of thermo-physical characterization of materials. In this case, heat conduction transfer was preponderant. In our study, we focus on heat transfer between a wall and its fluid environment. In this context, the proposed fluxmetric sensors were used in a limited amount of work, but are well adapted to the problem. In this work, the sensors are used to locally measure the convective and radiative transfer at the surface of a rectangular isothermal wall, a wall element of a rectangular horizontal channel. Experimental results are compared to those provided by the commercial, well-known CFD code Fluent. To do this, a case study is conducted experimentally and numerically with a forced convection turbulent flow fully developed in an open horizontal duct differentially heated in the measurement area located nearby the channel outlet. The radiative heat transfer, therefore, coexists with the convection heat transfer.

In these experiments, the heat fluxes are measured using fluxmeters [30], and the temperatures are measured using ∼0.1 mm diameter microthermocouples. Local velocities are measured with hot-wire anemometers. The Chebyshev log method [36] is used to obtain the flow rate and therefore the average velocity in a section of the channel. The overall goal is to validate the fluxmetric measurement techniques for the characterization of the surface heat transfer in a "simple" configuration. These sensors could then be used for more geometrically complex problems.

The rectangular heated wind tunnel is schematically depicted in Fig. 2, consisted of a test section instrumentation to measure heat flux in our experiments. The setup is placed in an isothermal room to prevent heat transfer with the external environment.

The channel length is 2.08 m and the straight section is rectangular (0.37×0.08 m^2). The channel is supplied by a variable-velocity fan (0–8 m/s); the channel inlet flow is made uniform by a converging device and a perforated gridding doubled with a layer of porous material.

A heat exchanger plate (25×30 cm^2) is inserted into the lower wall at 1.615 m downstream of the channel inlet in order to set it in a fully developed flow. At this distance from the inlet the flow is fully developed. This plate provides an isothermal plane through a thermostatically controlled bath regulating within 0.1 °C. To determine the heat flux in this channel, TGFMs of different dimensions are inserted rigorously flush in the lower plate to avoid disturbances. Fig. 2 shows the four different experiments that have been carried out for the study. The first experiment (a) is conducted with two identical fluxmeters (5×5 cm^2). The three other experiments (b–d) use ten rectangular fluxmeters of 1 cm wide and 15 cm long.

To ensure a uniform temperature over the whole plate, a thin copper plate is glued on the top of the heat exchanger plate, creating a thin 1 mm plate's thickness. This plate is covered with a coat of black matte paint $\varepsilon_f = 0.98$, absorbing heat flux radiation by an upper isothermal heating resistance (30×30 cm^2) placed opposite to the lower wall (Fig. 2).

This configuration allows generating heat transfer by radiation between both plates as well as implementing heat transfer by forced convection. In our various tests, the flow in the channel is dynamically developed and is turbulent and permanent. The measured signal is recorded every 2 s during 2 h, once the established regime reached. To evaluate the heat transfer in the channel, it is necessary to know the quantity of heat transferred at any time.

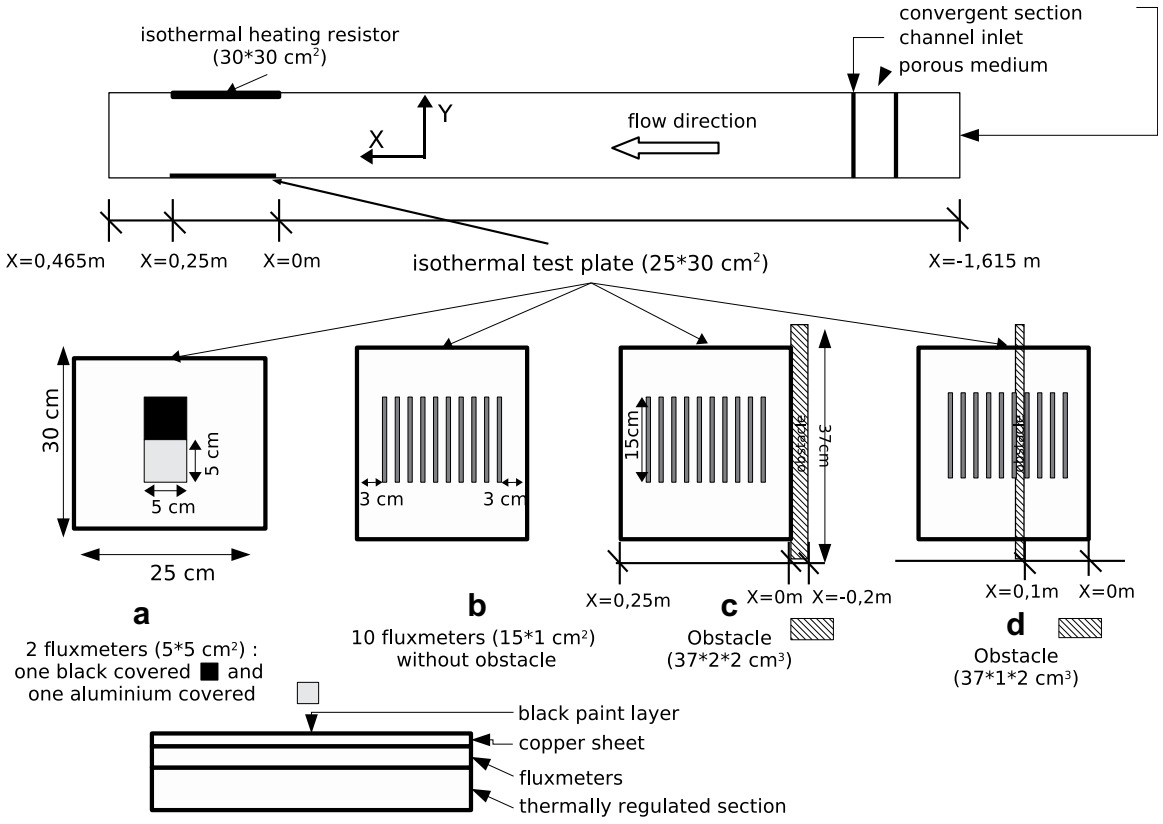

Fig. 2. Geometry of the channel (2D projection).

The fluxmeters described in this section allow recovering this information.

The metallic and conducting nature of the sensor's materials result in the sensor having little effect on the measured flux value, and this value is very close to what it would be without the sensor presence. When the flow is developed, measurements are taken upstream from the channel outlet using the various fluxmeters inserted into the lower plate which is thermally controlled at a constant temperature. This allows generating radiative heat transfer between these two horizontal surfaces. Contact between the fluxmeters and the heat exchanger plate is ensured by a thin silicone grease layer to limit the thermal contact resistance. The characteristic temperature variation between the "hot" upper plate T_1 and the "cold" lower plate T_2 is controlled by a computer and a PID regulator. Twelve *T*-type thermocouples precalibrated at ± 0.1 *K* are located at various sites in the channel to evaluate the air and wall temperatures. Moreover, they are also placed in different places on the two plates (upper and lower) in order to ensure them to be isothermal.

3. Governing equations and numerical method

We assume that the air in the duct is Newtonian and incompressible and the flow is governed by the steady three-dimensional Navier–Stokes equations. The working fluid is air ($Pr = 0.7$) coming into the channel at a constant ambient temperature.

The Reynolds number calculation is based on the hydraulic number $D_h = 0.13$ m.

$$Re = \frac{U_\infty \times D_h}{\nu} \tag{3}$$

Under the studied configurations, this number varies from $5.6.10^3$ to $3.5.10^4$, which corresponds to turbulent flow conditions. The simulations are conducted using the Fluent software. First, using the standard two-equations k–ε the turbulence model with enhanced wall treatment is tested. This model is based on the concept of turbulent viscosity. A second 'RNG' model (renormalization group) available under Fluent is tested, where the turbulent viscosity is calculated from a differential equation. This allows defining a relationship between the effective viscosity and the local Reynolds number. This model also allows partially taking into account the anisotropy and inhomogeneity of the turbulence near the wall. The application of this technique to the numerical resolution of turbulence was initiated by Ref. [37]. The results obtained from the k–ε model are presented in the first part of the study. In the second analysis, we will compare these two models of turbulence on heat transfer. Finally, for the last experiment, we will only focus on the results from the k–ε model. Forced convection with heat radiation for a turbulent flow in the horizontal duct is therefore solved using the following system of equations: mass conservation equation

$$\frac{\partial(\rho U_j)}{\partial x_j} = 0 \tag{4}$$

momentum conservation equation

$$\frac{\partial \rho U_i U_j}{\partial x_j} = -\frac{\partial P}{\partial x_i} + \frac{\partial\left(S_{ij} - \rho\overline{U_i' U_j'}\right)}{\partial x_j} \tag{5}$$

where

$$S_{ij} = \mu\frac{\partial U_i}{\partial x_j} + \mu\frac{\partial U_j}{\partial x_i} - \frac{2}{3}\mu\frac{\partial U_m}{\partial x_m}\delta_{ij}$$

and

$$\rho\overline{U_i'U_j'} = \mu_t\frac{\partial U_i}{\partial x_j} + \mu_t\frac{\partial U_j}{\partial x_i} - \frac{2}{3}\mu_t\frac{\partial U_m}{\partial x_m}\delta_{ij} - \frac{2}{3}k\delta_{ij}$$

$$\mu_t = \rho C_\mu\frac{k^2}{\varepsilon}$$

and

$$k = \frac{1}{2}\overline{u_i'^2}$$

turbulent energy transport equation

$$\frac{\partial}{\partial x_i}(\rho U_i k) = \frac{\partial}{\partial x_i}\left[\left(\mu + \frac{\mu_t}{\sigma_k}\right)\frac{\partial k}{\partial x_i}\right] + \mu_t\left(\frac{\partial U_i}{\partial x_j} + \frac{\partial U_j}{\partial x_i}\right)\frac{\partial U_j}{\partial x_i} - \rho\varepsilon \tag{6}$$

energy dissipation transport equation

$$\frac{\partial}{\partial x_i}(\rho U_i\varepsilon) = \frac{\partial}{\partial x_i}\left[\left(\mu + \frac{\mu_t}{\sigma_\varepsilon}\right)\frac{\partial \varepsilon}{\partial x_i}\right] + C_{\varepsilon 1}\frac{\varepsilon}{k}\mu_t\left(\frac{\partial U_i}{\partial x_j} + \frac{\partial U_j}{\partial x_i}\right)\frac{\partial U_j}{\partial x_i} - C_{\varepsilon 2}\rho\frac{\varepsilon^2}{k} \tag{7}$$

energy equation

$$\frac{\partial(\rho H U_j)}{\partial x_j} = -\frac{\partial}{\partial x_j}\left(\lambda\frac{\partial T}{\partial x_i}\right) + U_j\frac{\partial P}{\partial x_j} + S_{ij}\frac{U_j}{\partial x_i} + \frac{\partial}{\partial x_j}\left(-\rho\overline{U_j'h'}\right) \tag{8}$$

μ_t is the turbulent viscosity, constants are those used by Launder and Spalding [38]: $C_{\varepsilon 1} = 1.44$, $C_{\varepsilon 2} = 1.92$, $\sigma_k = 1$, $\sigma_\varepsilon = 1.3$ and $C_\mu = 0.09$. The radiative transfer equation is solved using the discrete ordinates model for a finite number of discrete finite angles (angular discretization S_4), each associated with a vector direction $\vec{s}$. Each octant of the angular space 4π at any spatial location is discretized into $N_\theta \times N_\Phi$ solid angles, called control angles. The angles θ and Φ are the polar and the azimuthal angles, and are measured in the cartesian system. In 2D calculations, only 4 octants are solved due to symmetry making a total of $4N_\theta N_\Phi$ directions. This method consists in evaluating angular integrals by means of numerical quadratures. The hemispherical angular space is discretized for a set of different directions. In our study, the hemispherical space has been divided into 64 directions. A study of sensitivity shows that it is sufficient and radiative heat flux is stable. radiative equation

$$\frac{\mathrm{d}\vec{I}_r}{\mathrm{d}s}(\vec{r},\vec{s}) + (a+\sigma_S)\vec{I}_r(\vec{r},\vec{s}) = \mathrm{an}^2\frac{\sigma T^4}{\pi} + \frac{\sigma_S}{4\pi}\int_0^{4\pi}\vec{I}_r(\vec{r}',\vec{s}')\phi(\vec{s},\vec{s}')\mathrm{d}\Omega' \tag{9}$$

To compare heat flux and temperature measurements, numerical 3D simulations of the problem were carried out using the Fluent computational fluid dynamics (CFD) software. The above described apparatus is discretized using the built-in modeller Gambit which provides the appropriate non-uniform Cartesian grids for the study.

The method of finite volumes with a structured meshing is used to solve the incompressible 3D Navier–Stokes equations. The convergence is checked by several criteria. All the channel walls, which are isothermal, are assumed to be at the ambient air temperature T_0, except for the two plates concerning our measurements which are at a different imposed temperature. We impose at the inlet a uniform velocity profile and we obtain at the outlet a free flow at atmospheric pressure.

The conservation equations are discretized on a hexahedron grid using a finite volume procedure. The resolution is based on a steady 3D model using various schemes such as the upwind scheme of second order for the convective terms of the momentum equation, the energy equation and the two-equations related to the k–ε turbulence model. A SIMPLE (semi-implicit method for pressure linked equations) method proposed by Patankar and Spalding [39] was employed to solve the coupling between pressure and velocity. The momentum, the turbulence kinetic energy, the turbulence dissipation rate, and the energy equations are discretized using a second order upwind scheme. Under-relaxation coefficients were found to be required to control the advancement of the solution field without spurious and undesirable oscillations. A grid refinement around the zone of measurement was proposed to determine the adequacy of the mesh scheme and to ensure that the solutions are grid independent.

4. Results and discussions

4.1. Numerical tests

Four grid sizes were evaluated as shown in Fig. 3, and have been tested to ensure the results are grid independent. For this study, an experiment has been chosen among others to show the results. To achieve that, ten heat flux sensors (15 cm long and 1 cm wide) are rigorously inserted into the lower heat exchanger plate to limit the wall ruggedness effects. They are placed transversely to the flow as shown in Fig. 2(b). To track the spatial behavior over almost all the heat exchanger plate surface (purpose of the next tests), the ten fluxmeters are uniformly spaced 1 cm apart. These fluxmeters are covered with a thin coat of black matte paint ($\varepsilon_f = 0.98$) in order to obtain a direct measurement of the total heat flux along the plate.

In Fig. 3, heat fluxes are plotted versus the flow direction over the fluxmeters depicted in Fig. 2(b) for $Re = 10{,}400$. The non-uniform grids involve respectively 66,600, 124,714, and 164,714 control volumes.

As shown in Fig. 3, increasing the grid size above 124,714 elements does not significantly change the heat flux prediction over the plate for $Re = 10{,}400$. Several other tests were carried out for variable Reynolds number with similar results.

Note that the relative discrepancy between the experimental and the numerical results lies between 1% and 4%. Standard wall

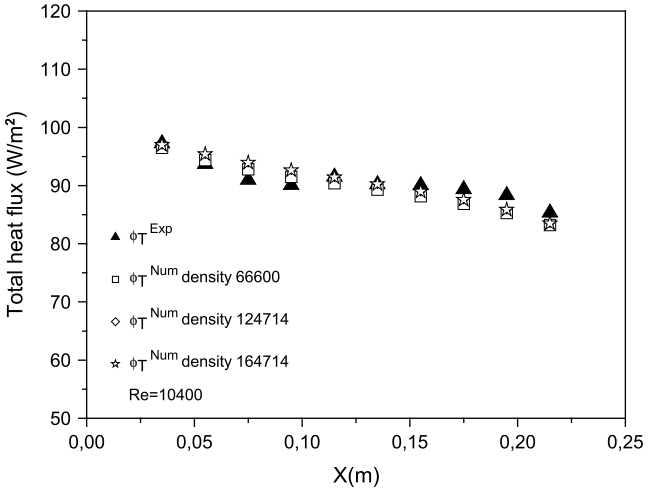

Fig. 3. Grid sensitivity test, $Re = 10{,}400$, $T_0 = 297$ K and $T_2 - T_1 = 13$ K.

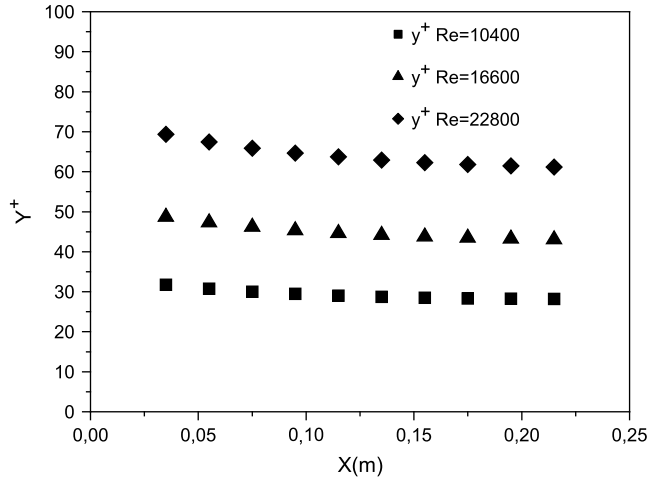

Fig. 4. Y^+ values in the flow direction for $Re = 10{,}400$, 16,600, and 22,800.

functions have been used throughout the test procedure. These acknowledged functions have been successfully used in numerous industrial applications [38]. For a convenient simulation, Fluent requires to set some prescribed conditions ; the Y^+ value has to be set between 30 and 300 [40], with:

$$Y^+ = U_\tau \times Y_p \nu \tag{10}$$

where U_τ is the friction velocity and Y_p is the distance to the wall. Y^+ is a mesh dependent dimensionless length that quantifies to what degree the wall layer is resolved. For a turbulent region, Y^+ has to be more than 30. This condition is verified in order to analyze two different turbulence models, the k–ε model with a standard wall function and the RNG k–ε with a standard wall function. Fig. 4 shows the Y^+ values over the ten fluxmeters for three Reynolds numbers. As can be observed, the Y^+ values range between 29 and 75, this permits the use of a turbulence model with a standard wall function and furthermore it enables to obtain numerical results at relatively low computational cost.

After this test pertaining to the appropriateness of the use of a standard wall function, the 3D numerical simulations are compared with experimental results in attempts to select the best turbulence model to simulate the flow and the heat transfer in the channel. The RNG k–ε model and the k–ε model are hence used with wall treatment.

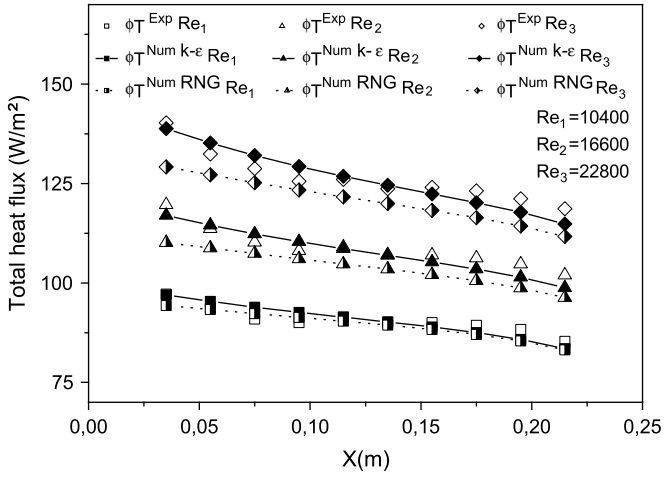

Fig. 5. Total heat flux in the X flow direction for $Re_1 = 10{,}400$, $Re_2 = 16{,}600$ and $Re_3 = 22{,}800$, $T_0 = 296\ K$ and $\Delta T = 12$ K.

Fig. 5 illustrates the results for three different values of Reynolds number and small temperature differences. Air temperature T_0 is 296 K, cold isothermal plate $T_1 = 291.6\ K$ and hot resistor temperature $T_2 = 303.5\ K$. Fig. 5 represents the spatial evolution of the heat flux in the flow direction. The comparison of the results provided by the two models of turbulence reveals a coherent numerical prediction with measurements. On the quantitative level, the RNG k–ε prediction curves are always below the standard k–ε curves which provide predictions closer to the experimental measurements. The maximal relative discrepancy with experimental data is not higher than 5%. Therefore, although the k–ε and RNG k–ε models provide realistic predictions of the heat flux, in the following section, all the results are presented for the k–ε model which is found better here.

4.2. Separation of the heat fluxes coupled by convection and radiation

The heat flux sensors described in the previous section measure the heat flux corresponding to the evaluation of convective and radiative transfer between their support walls and their environment. The objective of this study is to quantify the convective component and the radiative component of the total heat flux received on the lower heat exchanger plate. To do this, we symmetrically insert two flux sensors of the same design ($5 \times 5\ \mathrm{cm}^2$) into the cold lower plate acting as a thermal wall (Fig. 2a).

We know that the total transferred heat flux between the two plates ϕ_T represents the sum of the convective heat flux ϕ_C and the radiative heat flux ϕ_R

$$\phi_T = \phi_C + \phi_R \tag{11}$$

The approach used to split the total flux into a convective component and a radiative component consists of changing the emissivity of each fluxmeter's surface [41]. One of the two sensors is thus covered by a thin "absorbing" coating (black paint) of the same emissivity as the support plate such that its emissivity is close to 1 ($\varepsilon_f = 0.98$). As a result, this fluxmeter detects all the radiation transferred between the heat source and the cold support plate, as well as the convective flux transferred between the lower plate and the air.

The second sensor is covered with a thin aluminium foil of very low emissivity close to 0 ($\varepsilon_f = 0.1$) in order to reduce the radiative absorption as much as possible, the radiative transfer coefficient approaching toward zero.

Nevertheless, the heat flux value measured by this sensor ϕ_C takes into account a low radiative component ϕ_C^R due to a non-zero emissivity of this sensor. Thus, it is necessary to quantify this flux value ϕ_C^R. This radiative component of the flux measured by the reflecting sensor is calculated by the classical radiosity method, and also by numerical simulation using the Fluent software, using the discrete ordinates method.

$$\phi_C^C = \phi_C - \phi_C^R \tag{12}$$

In the radiosity method, it is assumed that the surfaces are isothermal and that the radiative properties are independent of the wavelength and of the direction. The channel is split into n elementary surfaces S_i, where $i = 1,\ldots, n$, and the following equation is solved

$$\sum_{j=1}^{n} [\delta_{ij} - (1-\varepsilon_i)F_{ij}]J_j = \varepsilon_i \sigma T_i^4 \tag{13}$$

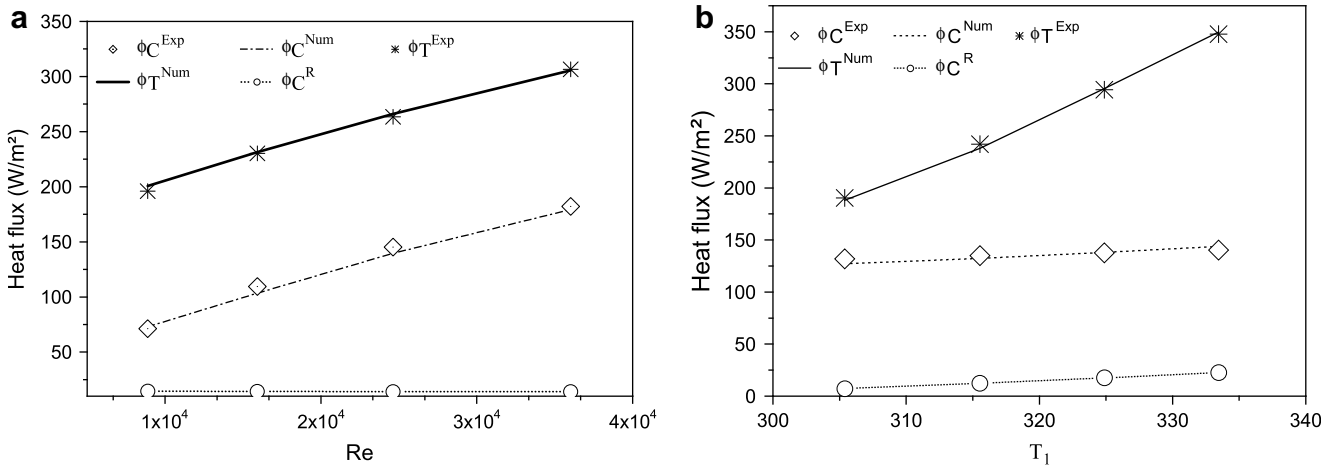

Fig. 6. Thermal heat flux: numerical total flux (solid), numerical convective flux (dash-dotted) versus Reynolds number *Re* (a) and versus temperature T_1 (b), and the dotted line with circles shows the results coming from the radiosity calculus, with $T_2 = 290$ K, $T_0 = 297$ K. $T_1 = 318$ K (a), $Re = 35{,}100$ (b).

where F_{ij} are the channel shape factors determining the joint effect of surfaces with respect to others, calculated as follows:

$$F_{ij} = \frac{1}{S_i}\int_i \int_j \frac{\cos\theta_i \cos\theta_j}{\pi l^2}\, dS_i dS_j \tag{14}$$

J_j being the radiosity of the surface S_j, ε_i the emissivity of the surface S_i and σ the Stefan–Boltzmann constant.

To illustrate our results on the heat flux, two different experiments have been conducted.

Fig. 6(a) shows the values of heat flux versus Reynolds number. The temperatures within and outside the channel are assumed to remain constant during the experiment. Note that the total flux and the convective flux increase with the Reynolds number at a fixed temperature difference between the two parallel plates. The evolutions of the heat flux measured by the absorbing sensor and by the "reflecting" sensor are therefore similar.

The value of the radiative flux is experimentally evaluated by subtracting for each Reynolds number the total flux ϕ_T from the convective flux value:

$$\phi_R = \phi_T - \phi_C^C = \phi_T - \phi_C + \phi_C^R \tag{15}$$

A second experiment is carried out to show the behavior of the heat fluxes versus temperature at constant velocity. The following Fig. 6(b). shows these results.

The plotted curves show that the convective flux is not affected by the heat radiation between the two plates because the medium is transparent to radiation. This test reveals the effect of the heat gradient imposed between the two plates on the fluxes. These fluxes increase with the upper surface's temperature.

These experimental values are compared with those obtained with the Fluent software. The meshing's effect on the results was studied. The tests demonstrated that a gridding of about 10^5 cells is sufficient for the range of parameters considered in this problem. The adopted meshing is a structured type meshing and was constructed using the Gambit software, a Fluent mesher. The modeling and the boundary conditions reproduce as accurately as possible the open channel of the experiment.

To analyse if the results are emissivity independent, an experiment has been carried out consisting in changing the numerical value of emissivity of the black painted sensor of the present experiment. Emissivity varies from 0.9 to 1 every 0.02 (Fig. 7). Results for total heat flux versus Reynolds number are shown in this figure. Increasing the magnitude of emissivity tends to increase the total heat flux. One can notice that the experimental value is close to the numerical curve of magnitude $\varepsilon_f = 0.98$. It agrees with the value chosen in the previous computations.

To conclude, the results obtained are extremely satisfactory. The relative error on the total and convective fluxes found between the experimentation and the numerical calculation in our different experiments is 5% maximum.

This experiment allowed us to locally uncouple the components of heat transfer in the channel, but could not provide us with any information about the spatial evolution of the heat flux in the duct.

4.3. Spatial evolution of total heat flux in the flow direction

To characterize the evolution of the total heat flux in the flow direction, various tests are carried out in the channel. A first experiment is carried out to observe the evolution of the total flux versus temperature at constant velocity. One can notice in Fig. 8(a) that the heat flux increases with increasing the upper plate temperature. The following curve in Fig. 8(b) shows the heat flux measured by each fluxmeter and represents its spatial behavior for several flow velocities. As in the previous experiment, the heat flux is averaged over the sensor's whole surface. Fig. 8(b) indicates a monotonic decrease in the total flux in the flow direction at

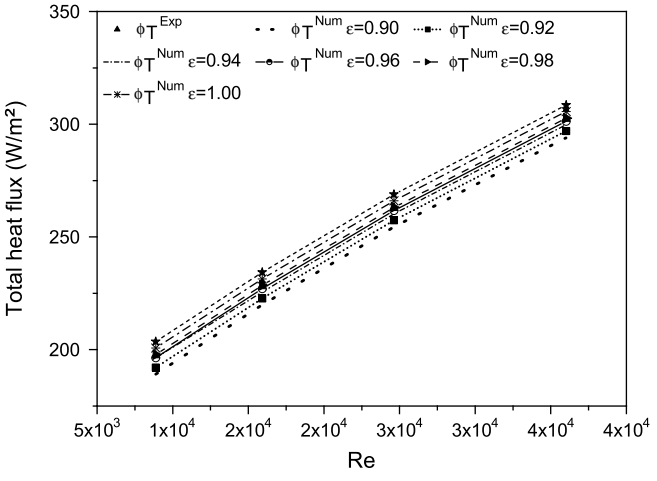

Fig. 7. Influence of the emissivity on the total heat flux.

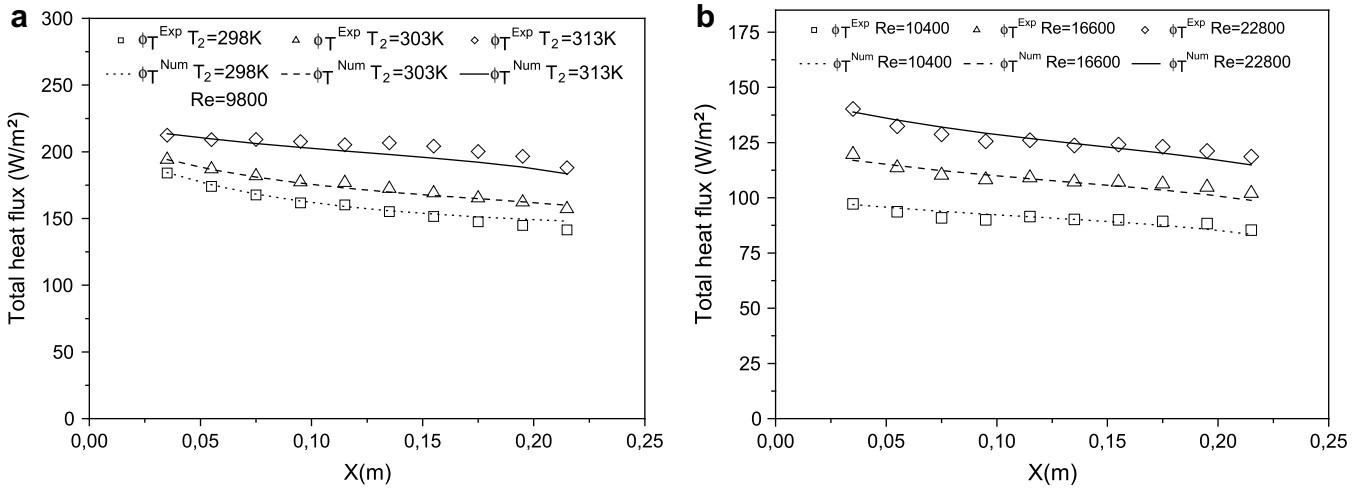

Fig. 8. Total heat flux in the X flow direction, $T_0 = 296$ K, $Re = 9800$ (a), $T_1 = 291.6$ K and $T_2 = 303.5$ K (b). .

constant temperature and velocity due to an increase of the thickness of the thermal boundary layer. With a constant temperature difference between the two plates, that is, for a constant impinging radiative flux, the total heat flux increases with velocity; the convective component of the flux is the component which governs the evolution.

The convective heat flux variation with respect to the *X–axis* is shown in Fig. 9, while the radiative heat flux variations are the subject matter of the results presented in Fig. 9(b).

Consequently, there is a direct consequence over the ratio of the radiative flux to the total flux. Fig. 9(b) indeed shows that the radiative flux is independant of the flow velocity and symmetric with respect to the center of the lower plate. Here, the ratio of the radiative flux to the total flux varies between 48 W/m^2 on the edges and 52 W/m^2 in the center of the plate.

Another check is carried out in order to ensure the validity of the proposed predictions. Both the numerical and experimental results are compared to the acknowledged Colburn's correlation. The parameter which is compared is the local Nusselt number. The following Fig. 10 shows the experimental and numerical local Nusselt number Nu_x for three different values of the Reynolds number. Results indicate that the solutions proposed herein are in good agreement with those reported by Ref. [1] who presented the Colburn's correlation.

$$Nu_x = 0.0296 \times Re_x^{4/5} \times Pr^{1/3} \tag{16}$$

4.4. Increase in heat transfer in the presence of an obstacle

The next experiments are concerned with the evolution of the total heat flux in the presence of an obstacle (37 cm wide $\times$ 2 cm high $\times$ 2 *cm* thick) placed transversely on the lower isothermal plate inlet (Fig. 2(c)).

The purpose of this series of measurements is to quantify the heat transfer increase due to the presence of an obstacle. However, the paper does not discuss the effect of the obstacle's geometry (cross section) on the heat transfer rates. Solution independence with grid refinement (both angular and directional) was verified. The number of control volumes used in this section is 141,053, while an S_4 angular discretization was used. Numerical simulations involving the k–ε model were obtained and the results are presented in Fig. 11(a) and (b) along with corresponding experimental results.

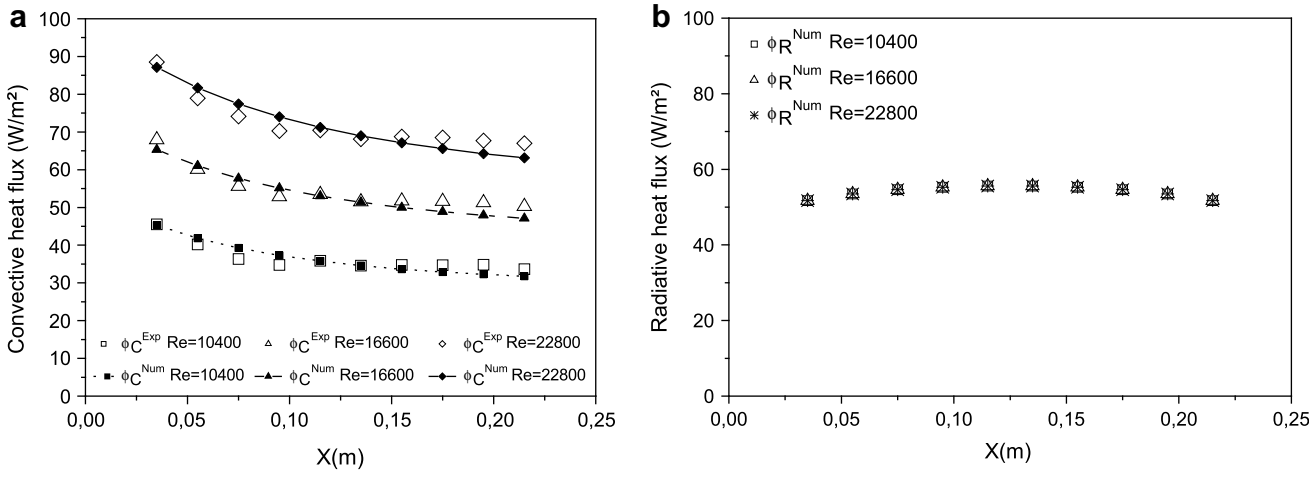

Fig. 9. Heat flux in the X flow direction $Re = 10{,}400$ (dotted line), $Re = 16{,}600$ (dashed line) and $Re = 22{,}800$ (solid line). $T_0 = 295.7$ K, $T_1 = 291.6$ K and $T_2 = 303.5$ K. Convective heat flux (a) and radiative heat flux (b).

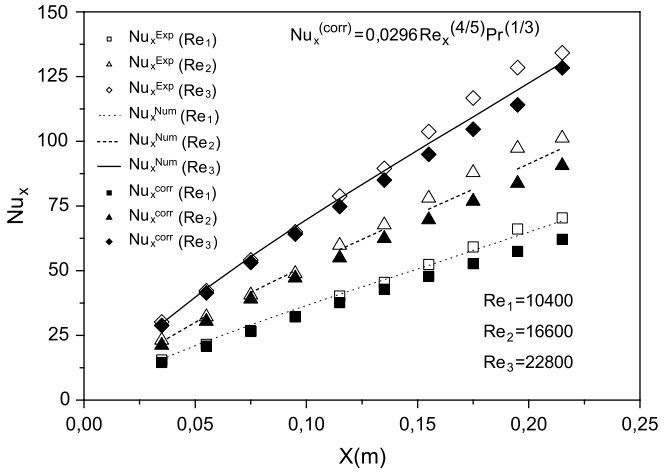

Fig. 10. Local Nusselt number for three different Reynolds numbers ($Re_1 = 10{,}400$, $Re_2 = 16{,}600$, and $Re_3 = 22{,}800$).

The separation zone, in the immediate vicinity of the obstacle, is an area of minimum heat transfer, while the reattachment zone, located further downstream, constitutes a more important heat transfer area. Heat transfer is expected to increase in the region where the viscous sublayer develops. Fig. 11(a) clearly reflects the above-discussed physics. The obstacle's wake is shown to cause a turbulent motion in the flow, thus improving overall convective heat transfer. The most important gap between experimental results and numerical ones is located in the separation zone, corresponding at the onset of the isothermal plate. Whereas at the end of the cold plate, far away from the obstacle, this difference decreases (about 1%). Therefore, this work is of interest for the study of heat transfer and opens a perspective for the development of our present study. However, a numerical effort must be carried out to improve the results obtained close to the obstacle.

Fig. 11(b) shows an increase in heat transfer versus temperature. At the fifth fluxmeter, the exchanged heat reaches its maximal value, and then decreases until the exit of the channel's plate. The relative variation between numerical and experimental results is less than 6%. Fig. 11(b) emphasises the influence of the radiation in this area. When the resistance's temperature increases, a gap is created, as in the previous figure, in the separation zone between experimental and numerical results with a maximum of 13%. As for Fig. 11(a), one can notice that the more the distance is long between the obstacle and the recorded flux value, the more the numerical–experimental difference is weak.

In the ultimate test presented here, the location of the obstacle is modified in order to highlight the flow recirculation effects on heat transfer. The width of the obstacle is decreased to 1 cm so as to fit it between the fourth and the fifth fluxmeters (from $X = 0.10$ m to $X = 0.11$ m), Fig. 2(d). As in the previous experiments, the test zone is submitted to forced convection as well as radiation. Experimental and numerical results are plotted in Fig. 12. There is an important change in thermal exchanges upstream of the obstacle (maximal value right at the fourth fluxmeter). A large and abrupt decrease of the overall heat flux is shown as soon as the flow passes over the edge of the obstacle. The thermal flux then rises until the exit of the plate, location of the second recirculating zone with negative velocities. The numerical and experimental results show a similar evolution. Nevertheless, one can notice a significant difference between the values predicted and those that were measured. The maximum discrepancies occur near the sixth fluxmeter. This is due to the interaction between negative velocities of some fluid particles which come back to the obstacle, and positive velocities of the turbulent fluid in this area. The highest relative difference found is 18%. Insufficient grid refinement was suspected here and the results are shown for two different grid refinements. Unfortunately, we were not able to refine the grid further as the capacity of our machines were pushed to their limits. This should now be investigated more thoroughly.

From the simulation point of view, parametric studies on the design assumptions (turbulence models, radiation, etc.) were realized and also the study of sensitivity to experimental parameters (temperatures, emissivity, etc.) [42]. It is thus noted that the obtained results (without obstacle) by the experimentation and calculation are in good agreement. The variation is less than 5%.

If an obstacle disturbing the flow, and consequently the heat transfer, is placed upstream the cold plate or between two fluxmeters in the middle of the lower plate, transversely to the air flow, the numerical simulation becomes very difficult in particular because of turbulence structures of dimensions close to the sensors ones, which average heat transfer over their whole surface. The relative variations between experiment and simulation are more

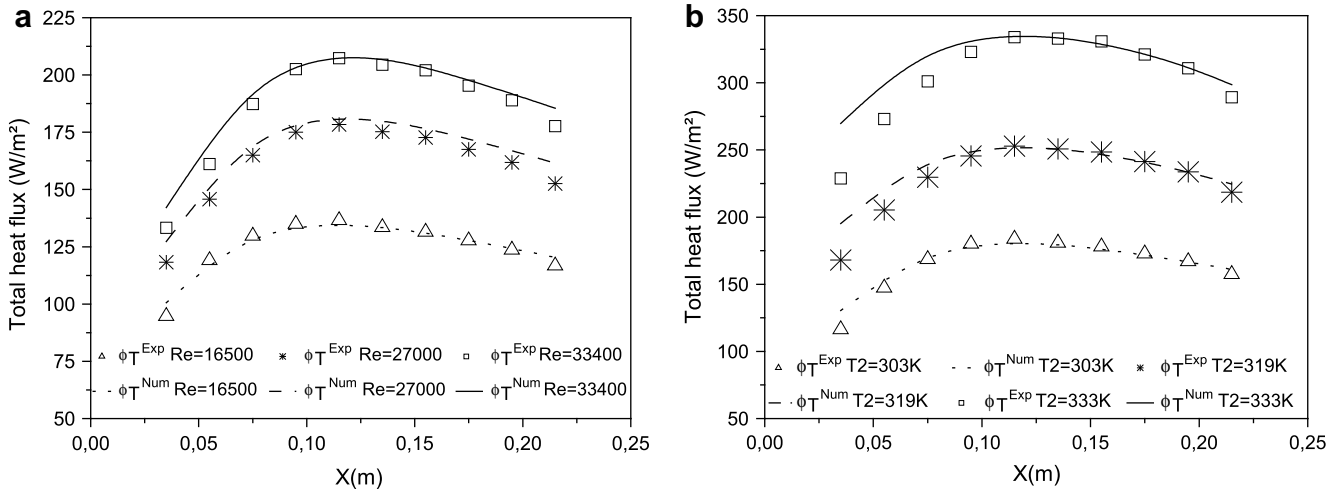

Fig. 11. Total heat flux in the X flow direction behind the solid body with $T_0 = 296$ K. $\Delta T = 13$ K (a) and $Re = 24{,}100$ (b) .

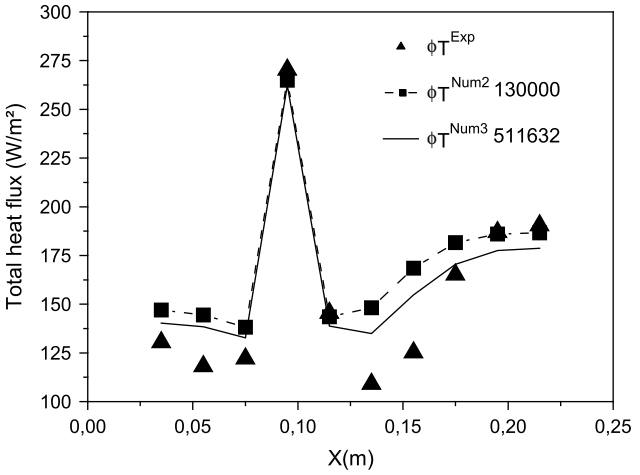

Fig. 12. Total heat flux in the flow direction behind the solid body located between the fourth and the fifth heat flux sensor. $T_1 = 287.7$ K, $T_2 = 303.1$ K and $T_0 = 296$ K and $Re = 9670$.

important, at worst about 18% in the case of the obstacle placed in the middle of the plate. In this last case, the proximity of the sensors undoubtedly induces a modification of the boundary conditions. But the experimental tool is here very interesting because it gives information on the reality and the specificities of the heat transfer. At this stage, modeling is not efficient and requires to be improved. In particular, the grid refinement near the obstacle and the thorough examination of the boundary conditions must be required, inducing an important cost of calculation and heavy experimental investigations (thermography, etc.). Later work must be led to this subject. Fluxmetric measurements allow nevertheless in a relative simple way to realize work on heat transfer optimization by modifying (for example) the nature and the geometry of the obstacle.

5. Concluding remarks

The work presented in this paper has demonstrated successfully that it is possible to directly obtain accurate measurements of heat flux via our heat flux sensors. Forced convection heat transfer of air in a rectangular horizontal channel was investigated experimentally and numerically. A lower temperature-controlled horizontal plate and an upper heating resistor allow changing significantly the convective and radiative components of the transferred fluxes.

A differentially heated part of a horizontal duct has been investigated numerically and experimentally. Our aim is to provide high quality results in order to understand the easiness of use of the heat flux sensors. To this aim, an experiment was set up and a 3D computational code was used. Temperature and heat flux have been measured in the experiment and numerical simulations have been achieved. There is a good agreement between our measurements and our calculus. This configuration shows how these sensors can be used to obtain a direct and accurate knowledge of the heat powers exchanged between a surface and its environment.

The emissivity of the sensors is modified applying different painted coatings to separate the radiative component of high wavelength from the convective component of the surface heat flux.

In a second part, considering that the radiative component of the fluxes can be calculated with accuracy, several fluxmetric sensors are placed on a horizontal plate to observe and describe the distribution of local convective transfer on this surface. 3D numerical simulations carried out using the Fluent computational code are in good agreement with our experimental results. It shows the ability to quantify precisely the surface heat convection transfer. The developed model is general and it can be easily customized to describe heat transfer phenomena. Since no sophisticated numerical processing is required to exploit the measurements, we can envision conducting both the study of complex geometric configurations and non-stationary heat states in frequency ranges adapted to the instrumentation.

In the last section of this paper, an obstacle is placed transversely at the lower isothermal plate inlet. The experimental results obtained allow spatially describing the evolution of the surface heat transfer. The turbulence phenomena generated by the obstacle are averaged by the fluxmetric sensors. During the numerical simulation, an average flux is calculated and compared to the measurements. Here again results from experiments and numerical simulation are close. Therefore, the experimental technique appears to be extremely advantageous: it can be applied very well in any energy transfer control device and for the optimization of surface heat transfer (increase or decrease).

Acknowledgements

This work takes part of a Technologies Avancées pour les Transports (T.A.T.) action. Financial support of this research provided by the state of France and the Nord-Pas de Calais region (C.P.E.R.) are gratefully acknowledged.

References

[1] A. Bejan, Convection Heat Transfer, Wiley-Intersciences, 1994.
[2] J.P. Holman, Heat transfer, ninth ed. McGraw-Hill, NY, 2002, [chapters 5–7].
[3] F.P. Incropera, D.P. Dewitt, Fundamentals of heat and mass transfer, fourth ed. J WILEY and Sons, NY, 1996.
[4] N.M. Tsirel'man, Determination of the heat transfer coefficient from the law of constant-temperature front propagation, Journal of Engineering Physics 25 (2) (1973).
[5] H.J. Sternfield, J. Reinkenhoff, Technics for determining local heat transfer coefficient, AIAA Journal 15 (1) (1977).
[6] H.Y. Wong, The measurement of convective heat loss from a solid surface to an airstream, Journal of Physics E: Scientific Instruments 12 (1979).
[7] W.J. Parker, R.J. Jenkins, C.P. Butler, G.L. Abbot, Flash method in determining heat capacity and thermal conductivity, Journal of Applied Physics 32 (1961) 1679–1684.
[8] D. Petit, J. Dard, A. Degiovanni, Determination du coefficient d'echange entre un fluide et une paroi, Revue Générale de Thermique 238 (1981) 719–732.
[9] M. Lazard, S. Andre, D. Maillet, Diffusivity measurement of semi-transparent media: model of the coupled transient heat transfer and experiments on glass, silica glass and zinc selenide, International Journal of Heat and Mass Transfer 47 (3) (2004) 477–487.
[10] D. Demange, M. Bejet, Experimental and software tools to forecast radiative and conductive thermal transfer in partially transparent material deposed on rotating blades for turbine engine, Aerospace Science and Technology 8 (4) (2004) 321–331.
[11] G. Gaussorge, La thermographie Infrarouge, Lavoisier (1984).
[12] F. Papini, P. Gallet, Thermographie infrarouge – image et mesure, Masson, Collection Mesures Physiques, 1994.
[13] D.L. Balageas, D. Ory, Quelques ameliorations dans la determination des transferts convectifs à partir de la thermographie infra-rouge, La recherche Aerospatiale, Bulletin bimestriel, (Paris) 3 (May–Jun 1980) 213–219.
[14] A. El Abbadi, D. Bougeard, B Baudoin. Experimental study of heat transfer distribution on a single finned tube, fourth European thermal sciences conference, Birmingham; 2004.
[15] D.J. Crowther, J. Padet, Measurement of the local convection coefficient by pulsed photo-thermal radiometry, International Journal of Heat Mass Transfer 34 (12) (1991) 3075–3081.
[16] B. Remy, A. Degiovanni, D. Maillet, Mesure du coefficient d'échange pour des écoulements à faibles vitesses, Revue Générale de Thermique 397 (34) (1995) 28–42.
[17] J.V. Beck, B. Blackwell, C.R. ST. Clair, Inverse heat conduction, Ill-posed problem, Wiley, New York, 1985.
[18] C.H. Huang, M.N. Ozisik, Inverse problem of determining the unknown strength of an internal plane heat source, Journal of Franklin Institute 329 (1992).

[19] C.H. Huang, M.N. Ozisik, Inverse problem of determining unknown wall heat flux in laminar flow through a parallel plate duct, Numerical Heat Transfer, Part A 21 (1992).
[20] V.L. Pokhorriler, Using the solution to the reverse problem of heat conduction in the calculation of the heat transfer coefficient from temperature readings inside the body, Journal of Engineering Physics 23 (5) (1972).
[21] V.N. Kozlov, Calculation of the heat transfer coefficient from the temperature at points inside a plate, Journal of Engineering Physics 19 (1) (1970).
[22] J.R.K. Rowe, G.D. Lock, M.J. Owen, Transient heat transfer measurements using thermochromic liquid crystal: lateral conduction error, International Journal of Heat Fluid Flow 26 (2005) 256–263.
[23] J.W. Baughn, Liquid crystal for studying turbulent heat transfer, Journal of Heat Fluid Flow 16 (1995) 365–375.
[24] L. Huadong, V. Kottke, Visualisation and determination of local heat transfer coefficients in shell-and-tube heat exchangers for staggered tube arrangement by mass transfer measurements, Experimental Thermal and Fluid Science 17 (1998) 210–216.
[25] C.J. Kobus, Utilizing disk thermistor to indirectly measure convective heat transfer coefficients for forced, natural and combined (mixed) convection, Experimental Thermal and Fluid Science 29 (6) (2005) 659–669.
[26] M. Degenne, S. Klarsfeld ASTM STP 885, in: E. Bales, M. Bomberg, G.E. . Courville (Eds.), Building applications of heat flux transducers, American Society for Testing and Material, Philadelphia, 1985, pp. 163–171.
[27] Building applications of heat flux transducers. ASTM STP 885. Bales, Bomberg, Courville; 1985.
[28] D.J. Ortolano, F.F. Hines, A simplified approach to heat flow measurement, Advances in Instrumentation 38 (1983) 1449–1456.
[29] D.A. Ochaoa, W.J. Baughn, A.R. Byerley, A new technique for dynamic heat transfer measurements and flow visualization using liquid crystal thermography, International Journal of Heat and Fluid Flow 26 (2005) 264–275.
[30] D. Leclercq, P. Thery, Apparatus for simultaneous temperature and heat flux measurements under transient conditions, Review of Scientific Instruments 54 (1983).
[31] E. Antczack, Identification par impédance thermique, application à la caractérisation des géomatériaux, Thèse de doctorat de l'université d'Artois; 1996.
[32] D.L. Marinoski, S. Guths, F.O.R. Pereira, R. Lamberts, Improvement of a measurement system for solar heat gain through fenestrations, Energy and Buildings 39 (2007) 478–487.
[33] G. Delaplace, J.F. Demeyre, R. Guerin, P. Debreyne, J.C. Leuliet, Determination of representative and instantaneous process side heat transfer coefficients in agitated vessels using heat flux sensors, Chemical Engineering and Processing 44 (9) (2005) 993–998.
[34] S.J. Kline, F.A. McClintock, Describing uncertainties in single sample experiments, Mechanical Engineering (1953).
[35] R.D. Orlandi, G.D. Derderian, L. Shu, B. Siadat. Calibration of heat flux transducers, building applications of heat flux transducers. ASTM STP 885, E. Bales, M. Bomberg and E Courville (Eds.), Philadelphia; 1985. pp. 65–78.
[36] J. Lefebvre. Mesure des debits et des vitesses des fluides (Ed) Masson; 1986.
[37] V. Yakhot, S.A. Orszag, Renormalization group analysis of turbulence, Journal of Scientific Computing 1 (1986) 1–51.
[38] B.E. Launder, D.B. Spalding, The numerical computations of turbulent flows, Computer Methods in Applied Mechanics and Engineering 3 (1974) 269–289.
[39] S.V. Patankar, Numerical heat transfer and fluid flow, Hemisphere, NY, 1980.
[40] Fluent 6.2 Documentation, Fluent Inc, 2003.
[41] S. Lassue. Analyse des échanges radiatifs et convectifs à la surface d'une paroi opaque. Application à la commande optimale du systeme habitat, These de doctorat de l'universite de Lille 1, 1989.
[42] Y. Cherif. Contribution à l'étude expérimentale et modélisation des transferts de chaleur par convection dans une lame d'air différentiellement chauffée, PhD, Université d'Artois; 2007.

Nomenclature

a: absorption coefficient [$m-1$]
C_μ, $C_{\varepsilon 1}$, $C_{\varepsilon 2}$: coefficients turbulence model
D_h: hydraulic diameter [m]
F_{ij}: shape factor of surface *i* with respect to surface *j*
h: heat transfer coefficient [$W\,m^{-2}\,K^{-1}$]
H: enthalpy [*J*]
I_r: total radiation intensity W/sr
I: electric current *A*
J: radiosity [$W\,m^{-2}$]
K: sensitivity of the sensor $V\,m^2\,W^{-1}$
k: turbulent kinetic energy [$m^2\,s^{-2}$]
n: refractive index
Nu_x: local Nusselt number
P: pressure [*Pa*]
P_f: power developed in the heat resistor W
Pr: Prandtl number
Re: Reynolds number
s: path length
S: surface [m^2]
S_{ij}: mean strain rate tensor [s^{-1}]
s': scattering direction vector
T: temperature [K]
U_∞: velocity [$m\,s^{-1}$]
U: voltage across the main resistor *V*
V: voltage *V*
$\overline{U_i'U_j'}$: turbulent Reynolds stress tensor [$m^2\,s^{-2}$]
x, y, z: directions of rectangular coordinates

Greek symbols
δ_{ij}: Kronecker delta function
ϕ: heat flux [$W\,m^{-2}$]
ρ: fluid density [$kg\,m^{-3}$]
λ: thermal conductivity [$W\,m^{-1}\,K^{-1}$]
μ: dynamic viscosity [$kg\,m^{-1}\,s^{-1}$]
μ_t: turbulent dynamic viscosity [$kg\,m^{-1}\,s^{-1}$]
ε_f: emissivity
ε: turbulent energy dissipation rate [$m^2\,s^{-3}$]
σ_k, σ_ε: turbulent Prandtl numbers
σ_s: scattering coefficient [m^{-1}]
σ: Stefan–Boltzmann constant [$W\,m^{-2}\,K^{-4}$]
θ: angle
Φ: phase function
Ω': solid angle
ν: kinematic viscosity [$m^2\,s^{-1}$]

Subscripts
0: ambient temperature
1: refers to hotter wall
2: refers to cooler wall
i, j, m: (=1, 2, 3) components in the Cartesian coordinate system
R: radiative component
C: convective component
T: global component

Superscripts
C: convective component
R: radiative component